Structural Evolution of Plasma Sputtered Core-shell Nanoparticles for Catalytic Combustion of Methane

Xiaoning Guo, Pascal Brault, Guojuan Zhi, Amaël Caillard, Guoqiang Jin, Xiangyun Guo

Structural Evolution of Plasma Sputtered Core-shell Nanoparticles for Catalytic Combustion of Methane

Xiaoning Guo [a,c], Pascal Brault [b,*], Guojuan Zhi [a,c], Amaël Caillard [b], Guoqiang Jin [a], Xiangyun Guo [a,*]

[a] State Key Laboratory of Coal Conversion, Institute of Coal Chemistry, Taiyuan 030001, PR China

[b] GREMI UMR6606 CNRS - Université d'Orléans BP6744, 45067 ORLEANS Cedex2, France

[c] Graduate University of the Chinese Academy of Sciences, Beijing 100039, PR China

*Corresponding author.

Fax/Tel: +86-351 4065282

Email: xyguo@sxicc.ac.cn (X. Y. Guo)

Fax: +33- 2 38 41 71 54; Tel: +33- 2 38 41 71 25

Email: Pascal.Brault@univ-orleans.fr (P. Brault)

Abstract

Fe@Pd, Fe@Pt and Fe@Au core-shell nanoparticles supported by silicon carbide have been prepared by plasma sputtering deposition, and employed as the catalyst for methane combustion. The core-shell catalysts exhibit higher activities than single metallic catalysts due to surface alloying effects. With the surface alloying of the core-shell nanoparticles, Pd-O and Pt-O bonds become weak because the increasing of electron cloud density around Pd and Pt atoms due to the electron transfer from surface Fe to Pd or Pt atoms. Therefore, the activities of Fe@Pd/SiC and Fe@Pt/SiC increase with the reaction time. Whereas the activity of Fe@Au/SiC keeps invariant in the reaction due to the Fe@Au core-shell structure has high stability. Transmission electron microscopy and X-ray photoelectron spectroscopy results further confirm the structural evolution.

Keywords: Core-shell bimetallic catalysts; structural evolution; methane combustion, plasma sputtering deposition.

1. Introduction

Core-shell bimetallic nanoparticles have been extensively studied and widely applied in the heterogeneous catalysis, such as CO oxidation, oxygen reduction reaction and ethanol oxidation [1-7]. Usually, the shell layers of core-shell nanoparticles are noble metals; therefore the core–shell structures are ideal architectures for reducing dosage of noble metals and improving activity of catalysts. However, very few studies are devoted to investigating the stability of the core-shell structured nanoparticles in catalytic reactions especially under high-temperatures [8]. Moreover it

is argued that catalytic core-shell nanoparticles certainly are superior to other structures such as alloys. For example, Mizukoshi et al. claimed that Au/Pd random alloy supported on TiO_2 exhibited higher activity than TiO_2 supported Au@Pd core-shell nanoparticles in photochemical evolution of H_2 from ethanol aqueous solutions under UV illumination [9].

Various preparation techniques, such as sequential synthesis and arc discharge, have been proposed for preparation of core-shell structural catalysts [10-13]. Recently, plasma sputtering deposition has been studied extensively because the technique is feasible and no post-treatment is needed [14, 15]. Considerable studies are devoted to preparation of bimetallic nanoparticles, suggesting that the plasma sputtering deposition has obvious advantages in controlling the composition of bimetallic nanoparticles [16-18].

Catalytic combustion of lean natural gas and air mixture has attracted considerable attention because the process operates at low temperature and produces little NO_x emission [19-21]. Supported noble metals (Pd, Pt and Au) have been found to have high catalytic activities for the methane combustion [19,20,22]. However noble metals are very rare and expensive. Because the activities of different catalysts are mainly related to the surface composition of metallic particles, localizing noble metals as a thin shell on common metal cores is expected to not only reduce the dosage of noble metals but also enhance the catalytic activity.

In this work, we have prepared silicon carbide supported Fe@Pd, Fe@Pt and Fe@Au core-shell bimetallic nanoparticles using the plasma sputtering deposition

method and investigated the compositional and structural evolution of the different core-shell nanoparticles by transmission electron microscopy and X-ray photoelectron spectroscopy. The variation in the catalytic performance of the core-shell bimetallic catalysts reveals the structural evolution of core-shell nanoparticles in the reaction.

2. Experiments

2.1 Catalyst Preparation

Fe, Pd, Pt and Au sputtering depositions were performed in a cylindrical stainless steel low pressure transformer coupled plasma device. The experimental setup dedicated to the study has been described elsewhere [23, 24]. Briefly, argon plasma was created in a chamber using a planar external RF antenna (13.56 MHz, 300W). The substrate used in this work is high surface area SiC [25,26], which is prepared from a sol–gel and carbothermal reduction route and has a specific surface area of 50.8 $m^2 g^{-1}$ and a pore volume of 0.13 $cm^3 g^{-1}$. The plasma depositions were performed under P = 0.5 Pa and V_b = -200 V, where P is the Ar pressure (the base pressure is 5×10^{-5} Pa) and V_b is the bias voltage of metal targets. All the single metal targets are analytically pure (99.99%). The side length of Fe and Pt square targets is 25 mm; and the diameter of Pd and Au circular targets is 25 mm. For preparing core-shell structured nanoparticles, the deposition time was firstly set up as 20 minutes for Fe deposition and then 7.5, 7.5 and 3.75 minutes for Pd, Pt and Au deposition respectively. The corresponding samples are marked as Fe@Pd/SiC, Fe@Pt/SiC and Fe@Au/SiC. For comparison, single metallic catalysts were also prepared. The deposition time for Fe, Pd, Pt and Au is 50, 12.5, 12.5 and 6.25 minutes respectively. The corresponding samples are

marked as Fe/SiC, Pd/SiC, Pt/SiC and Au/SiC.

2.2 Catalytic test

The catalytic performance of different catalysts for methane combustion was carried out in a fixed-bed quartz reactor with an inner diameter of 8 mm at atmospheric pressure, and the mixture of O_2(20%)/CH_4(2%)/N_2(78%) was used as the feedstock. 100 mg of the catalyst was packed between two layers of quartz wool. The hourly space velocity was controlled to be 25000 h^{-1}. Since the deactivation of the SiC-supported catalysts usually demand a long time, a repeated heating-then-cooling cycle method was employed to estimate the stability of different catalysts [18,27,28]. In this method, the catalyst was programmed heated to a temperature at which the reaction obtained a near 100% methane conversion at a rate of 5 ^{o}C/min. In the heating process, the methane conversion was measured at different temperature. Afterward, the reactor was cooled down to the temperature at which the catalyst just became inactive, and then the next reaction cycle began again. Usually, one cycle need 4 hours to finish. The composition of effluent gases was analyzed by GC-14B gas chromatograph with TDX-01 column (used to separate H2, CO, CO2, O2 and CH4) and TCD detector.

2.3 Catalyst characterization

The loadings of different metals in the catalysts were determined by Perkin-Elmer ELAN 5000 inductively coupled plasma-mass spectroscopy (ICP-MS) instrument. The microstructures of the catalysts were analyzed by using JEM-2010 high-resolution transmission electron microscope (HRTEM). X-ray photoelectron

spectroscopy (XPS) spectra of the catalysts used at different temperatures were measured on an ESCALAB 3 MKII de VG spectrometer by using Mg Kα (15kV, 20mA) X-ray source.

3. Results and discussion

3.1 Catalytic performances

The metal loadings of different core-shell catalysts measured by ICP-MS are listed in Table 1. In the core-shell catalysts, the Fe loadings are around 0.18 wt.% and the noble metal loadings are around 0.33 wt.%. The metal loadings of pure-metal catalysts were also determined by ICP-MS, and are around 0.5 wt% (Table 2). From Table 1 and 2, the loadings of Pd, Pt and Fe in different catalysts have slight decreases after reaction because the volatilization of corresponding metal oxide.

Fig. 1 shows the catalytic performances of methane combustion on Fe/SiC, Pd/SiC and Fe@Pd/SiC. From Fig.1a, Fe/SiC is active only above 650 ^{o}C; the methane conversion could reach 100% at a temperature as high as 780 ^{o}C. The activity of Pd/SiC is far better than Fe/SiC. The methane conversion on Pd/SiC increases with the reaction temperature in a relatively low temperatures range. The methane conversion on Pd/SiC begins to decline when the temperature is higher than 550 ^{o}C mainly due to decomposition of the active phase PdO into Pd [29,30]. When employing Fe@Pd/SiC as the catalyst, the methane combustion occurs at about 320 ^{o}C and the methane conversion can reach up to 100% at 530 ^{o}C. Such low loadings of Pd (0.3%) in the Fe@Pd core-shell catalyst can thus exhibit higher catalytic activity than Pd/SiC (0.5%), indicating that the core-shell structure has played an important role in the

catalytic reaction. It is widely considered that the excellent catalytic performance of core-shell nanoparticles could be attributed to near surface alloy effects [31]. In the present catalyst, subsurface Pd and Pd-Fe interface layers could effectively affect the binding of adsorbates (CH_4 or O_2) to the Fe@Pd nanoparticle surface; and then the changes in binding enthalpies can enhance the activity of the catalyst in methane catalytic combustion process. The activity of Fe@Pd/SiC begins to decline at 570 ^oC which is slightly higher than that of Pd/SiC (550 ^oC), indicating that the Fe@Pd structure can effectively delay the declination temperature of Pd-based catalysts.

Fig. 1b shows the stability of Fe@Pd/SiC catalyst in the combustion of methane. Fe@Pd/SiC can keep the methane conversion at almost 100 % after 10 reaction cycles, indicating that high surface area SiC supported catalysts have excellent stability in methane combustion because the high thermal conductivity and chemical stability of the high surface area SiC, which can effectively hinder the sintering of active nanoparticles and thus stabilize them [18,28]. In addition, it can be obviously seen that the methane conversion of Fe@Pd/SiC at low temperatures (lower than the temperature for 100% methane conversion) increases with the cycling times. It is widely known that the activity and selectivity of catalysts extremely depend on their structures [8]. Therefore, the increase in the catalytic activity of Fe@Pd/SiC mainly results from the structural evolution of Fe@Pd core-shell nanoparticles in the catalytic process.

Fig.2 shows the catalytic performances of Pt- and Au-based catalysts for methane combustion. Fig.2a and 2b indicate that the core-shell catalysts exhibit slightly higher

catalytic activity than their corresponding single metallic catalysts. Fig.2c and 2d show the stabilities of Fe@Pt/SiC and Fe@Au/SiC catalysts in the catalytic combustion of methane. Both catalysts can reach a 100% methane conversion and remain unchanged after 10 reaction cycles. These indicate that the high surface area SiC catalyst support can effectively stabilize metallic nanoparticles. The activity of Fe@Pt/SiC increases with the cyclic times suggesting that the Fe@Pt core-shell structure may produce similar changes as Fe@Pd/SiC during the reaction (Fig.2c). However, the activity of Fe@Au/SiC remains almost unaffected, indicating that the Fe@Au structure can be very stable during the reaction (Fig.2d).

3.2 HRTEM characterization

Fig.3 shows HRTEM images of fresh and used Fe@Pd/SiC catalysts. From Fig.3a, the Fe@Pd core-shell structure can be clearly observed. Isolated Fe@Pd nanoparticles are highly dispersed on the SiC substrate with an average size of about 4.2 nm (Table 1). The lattice spacing of the shell layer metal is around 0.224 nm, which is indexed as Pd (111) plane. The Fe cores have an average diameter of about 2 nm and are coated with a 1.1 nm-thick Pd layer (Table 1). From Fig.3b, the nanoparticles are still uniformly dispersed on the SiC support after reaction. However, the Fe@Pd core-shell structure has obviously changed into FePd alloy structure. The lattice spacing of 0.222 nm is indexed as the (111) plane of FePd alloy [32]. For nanoparticles which contain at least two elements, the surface atoms usually tend to lower Gibbs free energy to keep the stability of particles [33]. In our sputtering experiment, Fe atoms are firstly deposited onto the SiC surface to form nanosized Fe cores. Then Pd atoms are deposited onto

the Fe-deposited SiC substrate, and then coat the Fe cores due to stronger Pd-Fe interaction than that of Pd-SiC [32]. However, the Gibbs free energy of Fe (~ 241 mJ/m^2) is lower than that of Pd (~ 272 mJ/m^2) [34]. Therefore, Fe atoms can continually move to the surface to lower the surface free energy of Fe@Pd nanoparticles, and form surface FePd alloy during the cyclic reaction.

Fig.4 shows HRTEM images of fresh and used Fe@Pt/SiC and Fe@Au/SiC catalysts. In these figures, the lattice spacings of nanoparticles are around 0.226, 0.223 and 0.234 nm, which correspond to Pt (111) plane, PtFe (111) plane and Au (111) plane, respectively [35]. The nanoparticles of different catalysts are still well dispersed. From Fig.4a and 4b, it is obvious that the Fe@Pt core-shell structure has changed into PtFe alloy after reaction because the Gibbs free energy of Fe is lower than Pt (~ 299 mJ/m^2) [34]. However, the Fe@Au core-shell structure can stably exist even through 10 cyclic reactions, due to the Gibbs free energy of Au (~ 177 mJ/m^2) being lower than Fe [34]. From Table 1 and the HRTEM images, the average sizes of metal nanoparticles in all catalysts only have a slight increase after 10 reaction cycles, indicating that high surface area SiC based catalysts have excellent stability.

3.3 XPS characterization

The XPS spectra of fresh and used Fe@Pd/SiC are shown in Fig.5 and the corresponding binding energies (BE) of each metal and the derived surface atomic ratios are presented in Table 3. Generally, the BE values of metallic Pd are in the range 334.7-335.5 eV for Pd $3d_{5/2}$ and 340.3-340.8 eV for Pd $3d_{3/2}$; whereas the BE values of Pd^{2+} are in the range 337.5-337.8 eV for Pd $3d_{5/2}$ and 342.1-342.6 eV for Pd

$3d_{3/2}$ [36-38]. From Fig.5a, The Pd BE values of fresh Fe@Pd/SiC are 335.8 and 341.2 eV, which are higher than the BE values of metallic Pd. The higher binding energies is the characteristic of Pd species with valence between 0 and +2 [39]. From Fig.5b, the concentration of Pd^0 is greater than Pd^{2+} after reaction. This is due to the decomposition of PdO into Pd. However, the BE values of Pd^0 and Pd^{2+} are lower than those of fresh Fe@Pd/SiC, mainly resulting form the core-shell structure being partly changed into FePd alloy. Fe atoms with lower Gibbs free energy continually migrate from core to Fe@Pd nanoparticle surface in the course of the cyclic reaction. Meanwhile, the introduction of Fe may increase the surrounding electron cloud density around Pd [40,41]. As a result, the corresponding peaks of Pd^0 and Pd^{2+} shift to lower binding energies. In addition, the main active phase of Pd-based catalysts for methane combustion is PdO, and the intensity of Pd-O bond determines the activity of catalyst [19,20]. The Pd-O bond can become weak when the electron cloud density around Pd atoms increases. Thus the CH_4 dissociation species on active sites are more easily oxidized by dissociated O species. Moreover, the products are also more easily desorbed from the active sites. As a result, the activity of Fe@Pd/SiC increases with the cyclic times.

The Fe $2p_{3/2}$ and Fe $2p_{1/2}$ BE values at 706.6 and 719.5 eV are attributed to metallic Fe; while the Fe $2p_{3/2}$ and Fe $2p_{1/2}$ at 711.3 and 723.9 eV are indexed to Fe^{3+} [42,43,44]. Therefore, the Fe component in fresh and reacted Fe@Pd/SiC exists as Fe^0 and Fe^{3+}. However, the intensity of Fe 2p peaks of used Fe@Pd/SiC is larger than the fresh one mainly because large quantity Fe atoms have migrated from cores to the surface of

Fe@Pd nanoparticles. The surface atomic ratios shown in Table 3 further confirmed this result.

Fig.6 and Fig.7 show the XPS spectra of fresh and used Fe@Pt/SiC and Fe@Au/SiC. The corresponding BE values are also listed in Table 3. The main Pt component of used Fe@Pt/SiC is Pt^0 because PtO and/or PtO_2 are easily decomposed into Pt at higher temperatures. The Pt BE values of used Fe@Pt/SiC are lower than those of the fresh one because the Fe@Pt core-shell structure has changed into FePt alloy. The main active phases in Pt-based catalysts for methane combustion are metallic Pt, which is different with Pd-based catalysts [20]. The increase of surface Fe atoms significantly weakens the Pt-O bond [45]. Therefore the gradually weakening of Pt-O bonds results in the increasing activity of Fe@Pt/SiC with the cyclic times. By comparing with the Fig.6c and 6d, it is obvious that the intensities of Fe 2p peaks in used of reacted Fe@Pt/SiC catalyst are also larger than those of the fresh one. No obvious changes can be seen from Fig.7, suggesting the Fe@Au core-shell structure does not change during the reaction.

Fig.8 shows the XPS spectra of O 1s in fresh and used Fe@Pd/SiC, Fe@Pt/SiC and Fe@Au/SiC. The O 1s BE value at about 529.1 eV is attributed to the lattice oxygen associated with metal oxides, whereas the O 1s BE value at about 531.6 eV is attributed to absorbed oxygen [46]. Compare Fig.8a and 8b, it can be seen that the BE values of O1s in Fe@Pd/SiC slightly shift to lower binding energies after reation. This further confirm that the increasing of surrounding electron cloud density around Pd decline the intensity of Pd-O bond and then lower the BE values of lattice oxygen.

From Fig.8c and 8e, only absorbed oxygen exited in fresh Fe@Pt/SiC and Fe@Au/SiC, suggesting that the metal components in both two fresh catalysts are metallic phase. In Fig.8d, the lattice oxygen Fe@Pt/SiC in used can be attributed to Fe-O; while the BE value of adsorbed oxygen has a little decrease mainly result from the Pt-O continually weaken during the reaction. There is no change of BE values in Fe@Au/SiC has been found from the Fig.8f, indicating that the Fe@Au core-shell nanoparticles are very stable in the methane catalytic combustion reaction.

4. Conclusion

Silicon carbide supported Fe@Pd, Fe@Pt and Fe@Au core-shell bimetallic catalysts were prepared by plasma sputtering deposition for methane catalytic combustion. All the core-shell catalysts exhibit higher activities than corresponding single metallic catalysts due to the near surface alloying effects. With the structural evolution of Fe@Pd and Fe@Pt nanoparticles from core-shell structure to alloy, the Pd-O and Pt-O bonds become weaker and weaker. As a result, the catalytic activities of Fe@Pd/SiC and Fe@Pt/SiC can increase gradually with the cyclic reaction times. XPS and HRTEM results further confirm that the surface Fe concentration of Fe@Pd/SiC and Fe@Pt/SiC continually increase and the core-shell structure gradually change into alloy structure during the reaction. Whereas the activity of Fe@Au/SiC is very stable due to the stability of the Fe@Au core-shell structure in the reaction.

Acknowledgments

The work was financially supported by NSFC (Ref. 20973190), the in-house research project of SKLCC (Ref. SKLCC-2008BWZ010), and the National Basic

Research Program (Ref. 2011CB201405).

References

(1) Enache, D. I., Edwards, J. K., Landon, P., Solsona-Espriu, B., Carley, A. F., Herzing, A. A., Watanabe, M., Kiely, C. J., Knight, D. W., Hutchings, G. J. *Science* **2006**, *311*, 362-365.

(2) Edwards, J. K.; Solsona, B. E.; Landon, P.; Carley, A. F.; Herzing, A. A.; Kiely, C. J.; Hutchings, G. J. *J. Catal.* **2005**, *236*, 69-79.

(3) Edwards, J. K.; Thomas, A.; Carley, A. F.; Herzing, A. A.; Kiely, C. J.; Hutchings, G. J. *Green Chem.* **2008**, *10*, 388-394.

(4) Yang, H. *Angew. Chem. Int. Ed.* **2011**, *50*, 2674-2676.

(5) Peng, Z. M.; Yang, H. *Nano Today* **2009**, *4*, 143-164.

(6) Hsieh, Y. C.; Chang, L. C.; Wu, P. W.; Chang, Y. M.; Lee, J. F. *Appl. Catal. B* **2011**, *103*, 116-127.

(7) Silva, J. C. M.; De Souza, R. F. B.; Parreira, L. S.; Teixeira Neto, E.; Calegaro, M. L.; Santos, M. C. *Appl. Catal. B* **2010**, *99*, 265-271.

(8) Tao, F.; Grass, M. E.; Zhang, Y. W.; Butcher, D. R.; Renzas, J. R.; Liu, Z.; Chung, J. Y.; Mun, B. S.; Salmeron, M.; Somorjai, G. A. *Science* **2008**, *322*, 932-934.

(9) Mizukoshi, Y.; Sato, K.; Konno, T. J.; Masahashi, N. *Appl. Catal. B* **2010**, *94*, 248-253.

(10) Dabbousi, B. O.; Rodriguez-Viejo, J.; Mikulec, F. V.; Heine,J. R.; Mattoussi, H.; Ober, R.; Jensen, K. F.; Bawendi, M. G. *J. Phys. Chem. B* **1997**, *101*, 9463-9475.

(11) Pastoriza-Santos, I.; Koktysh, D. S.; Mamedov, A. A.; Giersig, M.; Kotov, N. A.;

Liz-Marzan, L. M. *Langmuir* **2000**, *16*, 2731-2735.

(12) Teng, X. W.; Black, D.; Watkins, N. J.; Gao, Y. L.; Yang, H. *Nano Lett.* **2003**, *3*, 261-264.

(13) Liu, X. G.; Geng, D. Y.; Meng, H.; Cui, W. B.; Yang, F.; Kang, D. J.; Zhang, Z. D. *Solid State Commun.* **2009**, *149*, 64-67.

(14) Rabat, H.; Andreazza, C.; Brault, P.; Caillard, A.; Béguin, F.; Charles, C.; Boswell, R. *Carbon* **2009**, *47*, 209-214.

(15) Berthet, A.; Thomann, A. L.; Cadete Santos Aires, F. J.; Brun, M.; C. Deranlot,; Bertolini, J. C.; Rozenbaum, J. P.; Brault, P.; Andreazzaz, P. *J. Catal.* **2000**, *190*, 49-59.

(16) Zhang, H. X.; Wang, C.; Wang, J. Y.; Zhai, J. J.; Cai, W. B. *J. Phys. Chem. C* **2010**, *114*, 6446-6451.

(17) Ito, Y.; Miyazaki, A.; Valiyaveettil, S.; Enoki, T. *J. Phys. Chem. C* **2010**, *114*, 11699-11702.

(18) Guo, X. N.; Brault, P.; Zhi, G. J.; Caillard, A.; Jin, G. Q.; Coutanceau, C.; Baranton, S.; Guo, X. Y. *J. Phys. Chem. C* **2011**, *115*, 11240-11246.

(19) Ciuparu, D.; Lyubovsky, M. R.; Altman, E.; Pfefferle, L. D.; Datye, A. *Catal. Rev.* **2002**, *44*, 593-649.

(20) Gélin, P.; Primet, M. *Appl. Catal. B* **2002**, *39*, 1-37.

(21) Zwinkels, M. F. M.; Järås, S. G.; Menon, P. G.; Griffin, T. A. *Catal. Rev.* **1993**, 35, 319-358.

(22) Choudhary, V. R.; Patil, V. P.; Jana, P.; Uphade, B. S. *Appl. Catal. A* **2008**, *350*, 186-190.

(23) Rabat, H.; Brault, P. *Fuel Cells* **2008**, *8*, 81-86.

(24) Thomann, A. L.; Brault, P.; Rozenbaum, J. P.; Andreazza-Vignolle, C.; Andreazza, P.; Estrade-Szwarckopf, H.; Rousseau, B.; Babonneau, D.; Blondiaux, G. *J. Phys. D: Appl. Phys.* **1997**, *30*, 3197-3202.

(25) Jin, G. Q.; Guo, X. Y. *Micropor. Mesopor. Mat.* **2003**, *60*, 207-212.

(26) Guo, X. Y.; Jin, G. Q. *J. Mater. Sci.* **2005**, *40*, 1301-1303.

(27) Guo, X. N. ; Shang, R. J. ; Wang, D. H.; Jin, G. Q.; Guo, X. Y.; Tu, K. N. *Nanoscale Res. Lett.* **2010**, *5*, 332-337.

(28) Guo, X. N.; Zhi, G. J.; Yan, X. Y.; Jin, G. Q.; Guo, X. Y.; Brault, P. *Catal. Commun.* **2011**, *12*, 870-874.

(29) Farrauto, R. J.; Hobson, M. C.; Kennelly, T.; Waterman, E. M. *Appl. Catal. A* **1992**, *81*, 227-237.

(30) Ozawa, Y.; Tochihara, Y.; Nagai, M.; Omi, S. *Chem. Eng. Sci.* **2003**, *58*, 671-677.

(31) Wang, G. X.; Wu, H. M.; Wexler, D.; Liu, H. k.; Savadogo, O. *J. Alloys Compd.* **2010**, *503*, L1-L4.

(32) Sato, K.; Kovács, A.; Hirotsu, Y. *Thin Solid Films* **2011**, *519*, 3305-3311.

(33) Dai, H. J.; Rinzler, A. G.; Nikolaev, P.; Thess, A.; Colbert, D. T.; Smalley, R. E. *Chem. Phys. Lett.* **1996**, *260*, 471-475.

(34) Jiang, Q.; Lu, H. M. *Surf. Sci. Rep.* **2008**, *63*, 427-464.

(35) Zeng, H.; Li, J.; Wang, Z. L.; Liu, J. P.; Sun, S. H. *Nano Lett.* **2004**, *4*, 187-190.

(36) Nelson, A. E.; Schulz, K. H. *Appl. Surf. Sci.* **2003**, *210*, 206-221.

(37) Arai, H.; Machida, M. *Catal. Today* **1991**, *10*, 81-94.

(38) Gao, Z. H.; Liu, Z. C.; He, F.; Xu, G. H. *J. Mol. Catal. A* **2005**, *235*, 143-149.

(39) Babu, N. S.; Lingaiah, N.; Kumar, J. V.; Prasad, P. S. S. *Appl. Catal. A* **2009**, *367*, 70-76.

(40) Lambrou, P. S.; Efstathiou, A. M. *J. Catal.* **2006**, *240*, 182-193.

(41) Lambrou, P. S.; Savv, P. G.; Fierro, J. L. G.; Efstathiou, A. M. *Appl. Catal. B* **2007**, *76*, 375-385.

(42) Zhang, X. B.; Yan, J. M.; Han, S.; Shioyama, H.; Xu, Q. *J. Am. Chem. Soc.* **2009**, *131*, 2778-2779.

(43) Bi, Y. S.; Chen, L.; Lu, G. X. *J. Mol. Catal. A* **2007**, *266*, 173-179.

(44) Bajnóczi, É. G.; Balázs, N.; Mogyorósi, K.; Srankó, D. F.; Pap, Z.; Ambrus, Z.; Canton, S. E. ; Norén, K. ; Kuzmann, E.; Vértes A.; Homonnay, Z.; Oszkó, A.; Pálinkó, I.; Sipos, P. *Appl. Catal. B* **2011**, *103*, 232-239.

(45) Mahata, N.; Gonçalves, F.; Pereira, M. F. R.; Figueiredo, J. L. *Appl. Catal. A* **2008**, *339*, 159-168.

(46) Wang, S. P.; Zheng, X. C.; Wang, X. Y.; Wang, S. R.; Zhang,S. M.; Yu, L. H.; Huang, W. P.; Wu, S. H. *Catal. Lett.* **2005**, *105*, 163–168.

Sample	Metal loading (ICP-MS) (wt. %)								Nanoparticle size (TEM) (nm)		Shell thickness (nm)	
	Fe		Pd		Pt		Au					
	fresh	used	fresh	used	fresh	used	fresh	used	fresh	used	fresh	used
Fe@Pd/SiC	0.18	0.17	0.31	0.30					4.2	4.5	1.1	
Fe@Pt/SiC	0.16	0.16			0.33	0.31			3.4	3.6	0.9	
Fe@Au/SiC	0.18	0.17					0.33	0.33	4.5	4.8	1.2	1.3

Tables

Table 1 The loadings of different metals, the average size of nanoparticles and the shell thickness of Fe@Pd/SiC, Fe@Pt/SiC and Fe@Au/SiC.

Sample	Metal loading (ICP-MS) (wt. %)							
	Fe		Pd		Pt		Au	
	fresh	used	fresh	used	fresh	used	fresh	used
Fe/SiC	0.52	0.51						
Pd/SiC			0.49	0.48				
Pt/SiC					0.50	0.47		
Au/SiC							0.49	0.49

Table 2 The loadings of different metals of Fe/SiC, Pd/SiC, Pt/SiC and Au/SiC.

Table 3 Binding energies (eV) of Pd 3d, Pt 4f, Au 4f and Fe 2p and the surface atomic ratios of different fresh and used catalysts.

Sample	Binding energy (eV)										Atomic ratio
	Pd $3d_{5/2}$		Pd $3d_{3/2}$		Pt $4f_{7/2}$	Pt $4f_{5/2}$	Au $4f_{7/2}$	Au $4f_{5/2}$	Fe $2p_{3/2}$	Fe $2p_{1/2}$	Pd (Pt or Au) / Fe
Fresh Fe@Pd/SiC	335.8	337.6	341.2	342.6					706.5	719.5	69:31
Used Fe@Pd/SiC	335.4	337.0	340.7	342.3					711.3	723.9	51:49
Fresh Fe@Pt/SiC					71.6	75.2			706.6	719.5	70:30
Used Fe@Pt/SiC					71.1	74.8			711.4	723.8	46:54
Fresh Fe@Au/SiC							84.1	87.8	706.6	719.7	73:27
Used Fe@Au/SiC							84.0	87.9	711.3	724.0	71:29

Figure captions:

Fig.1 Catalytic activities (a) of Fe/SiC, Pd/SiC and Fe@Pd/SiC catalysts, and the stability (b) of Fe@Pd/SiC for methane combustion.

Fig.2 Catalytic activities of Pt/SiC and Fe@Pt/SiC (a), Au/SiC and Fe@Au/SiC (b) catalysts, and stabilities of Fe@Pt/SiC (c) and Fe@Au/SiC (d) for methane combustion.

Fig.3 HRTEM images of fresh (a) and used (b) Fe@Pd/SiC catalyst; and the size distribution of nanoparticles.

Fig.4 HRTEM images of fresh and used Fe@Pt/SiC (a and b) and Fe@Au/SiC (c and d) catalysts; and the size distribution of nanoparticles.

Fig.5 XPS spectra of Pd 3d (a and b) and Fe 2p (c and d) levels of fresh and used Fe@Pd/SiC.

Fig.6 XPS spectra of Pt 4f (a and b) and Fe 2p (c and d) levels of fresh and used Fe@Pt/SiC.

Fig.7 XPS spectra of Au 4f (a and b) and Fe 2p (c and d) levels of fresh and used Fe@Au/SiC.

Fig.8 XPS spectra of O 1s levels of fresh and used Fe@Pd/SiC (a and b), Fe@Pt/SiC (c and d) and Fe@Au/SiC (e and f).

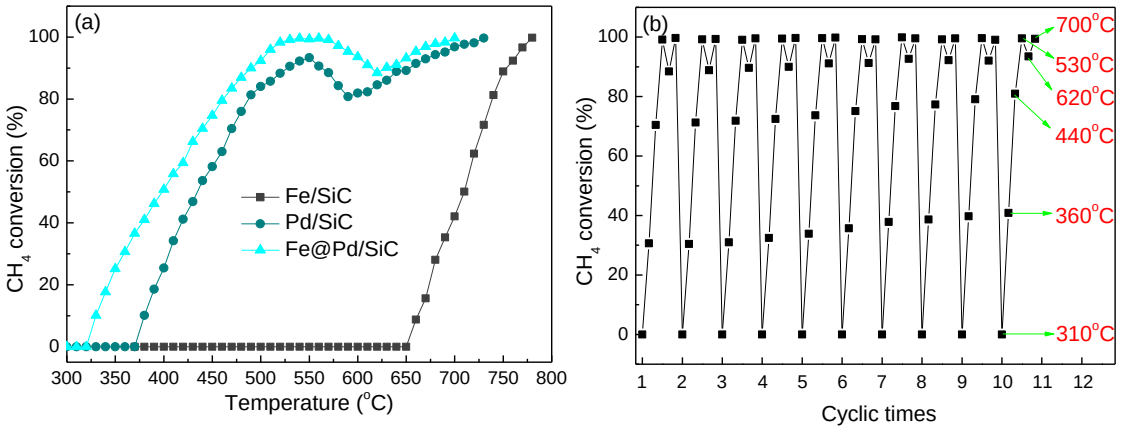

Fig.1 Catalytic activities (a) of Fe/SiC, Pd/SiC and Fe@Pd/SiC catalysts, and stability (b) of Fe@Pd/SiC for methane combustion.

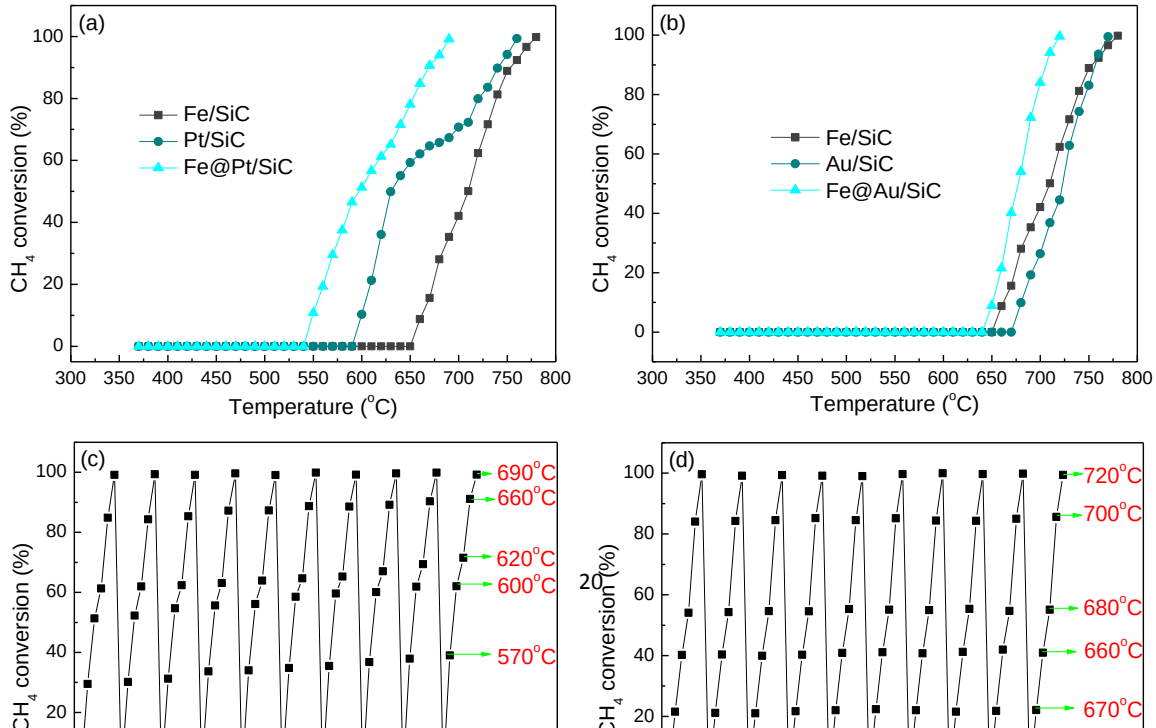

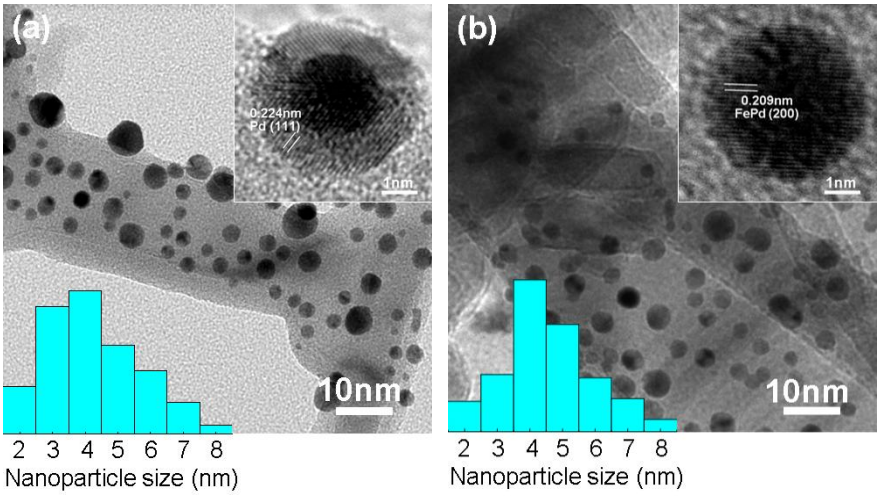

Fig.3 HRTEM images of fresh (a) and used (b) Fe@Pd/SiC catalyst; and the size distribution of nanoparticles.

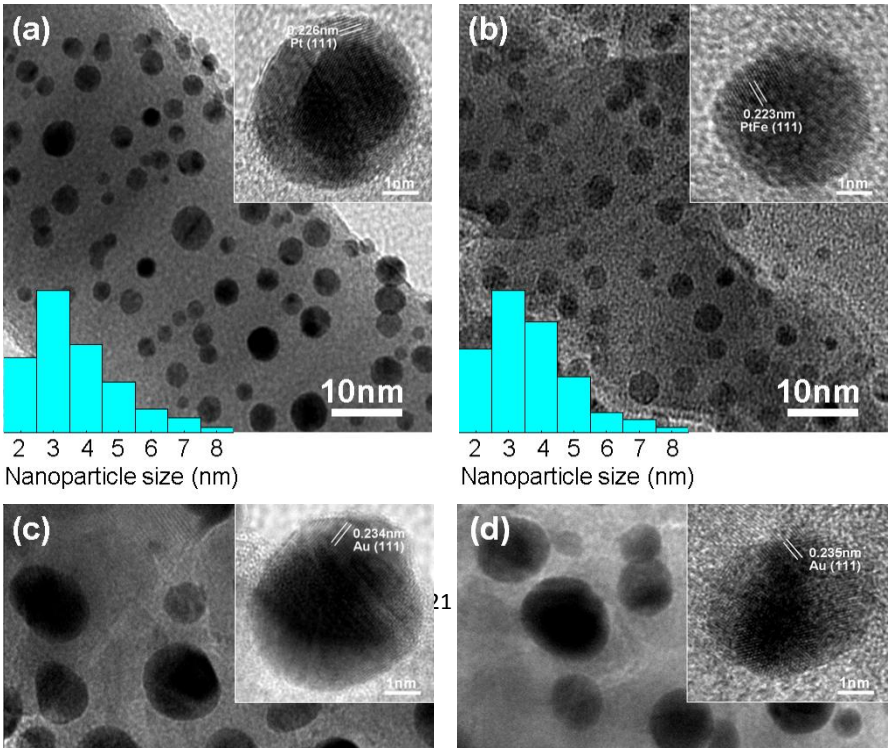

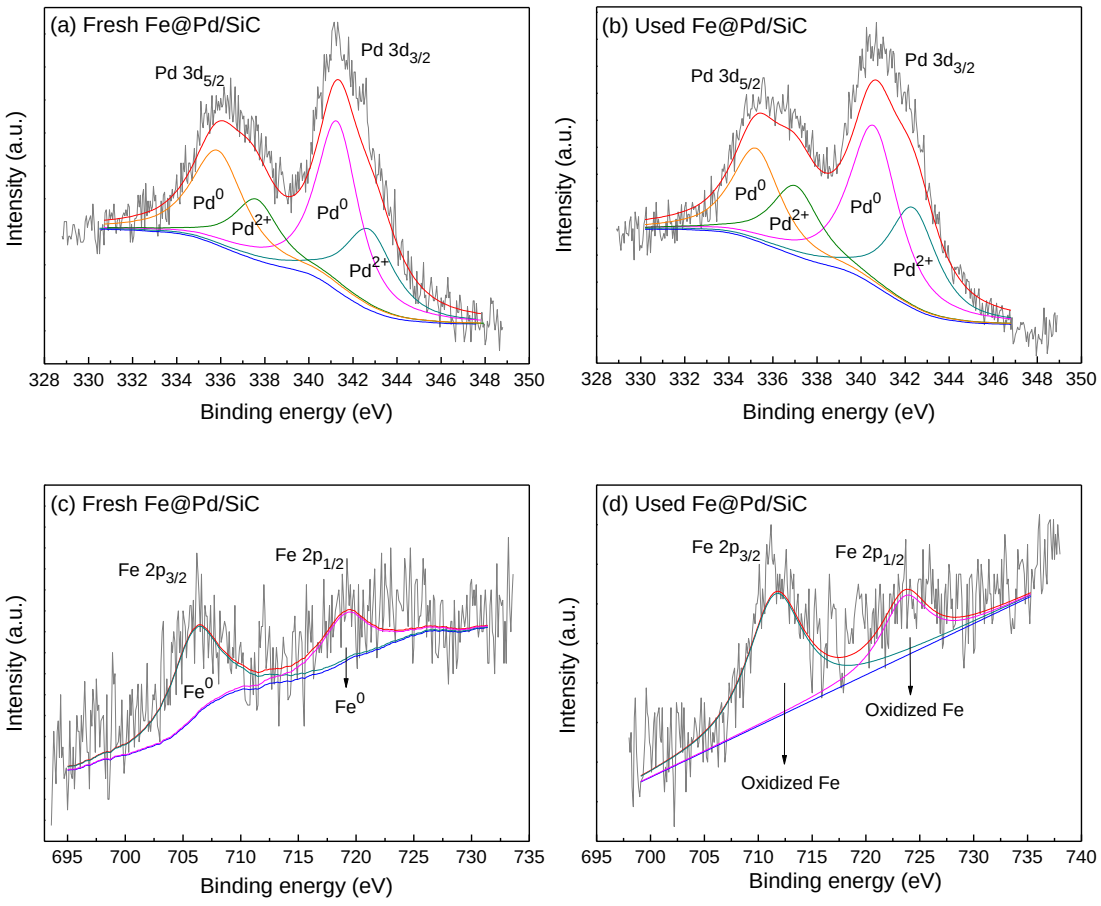

Fig.5 XPS spectra of Pd 3d (a and b) and Fe 2p (c and d) levels of fresh and used Fe@Pd/SiC.

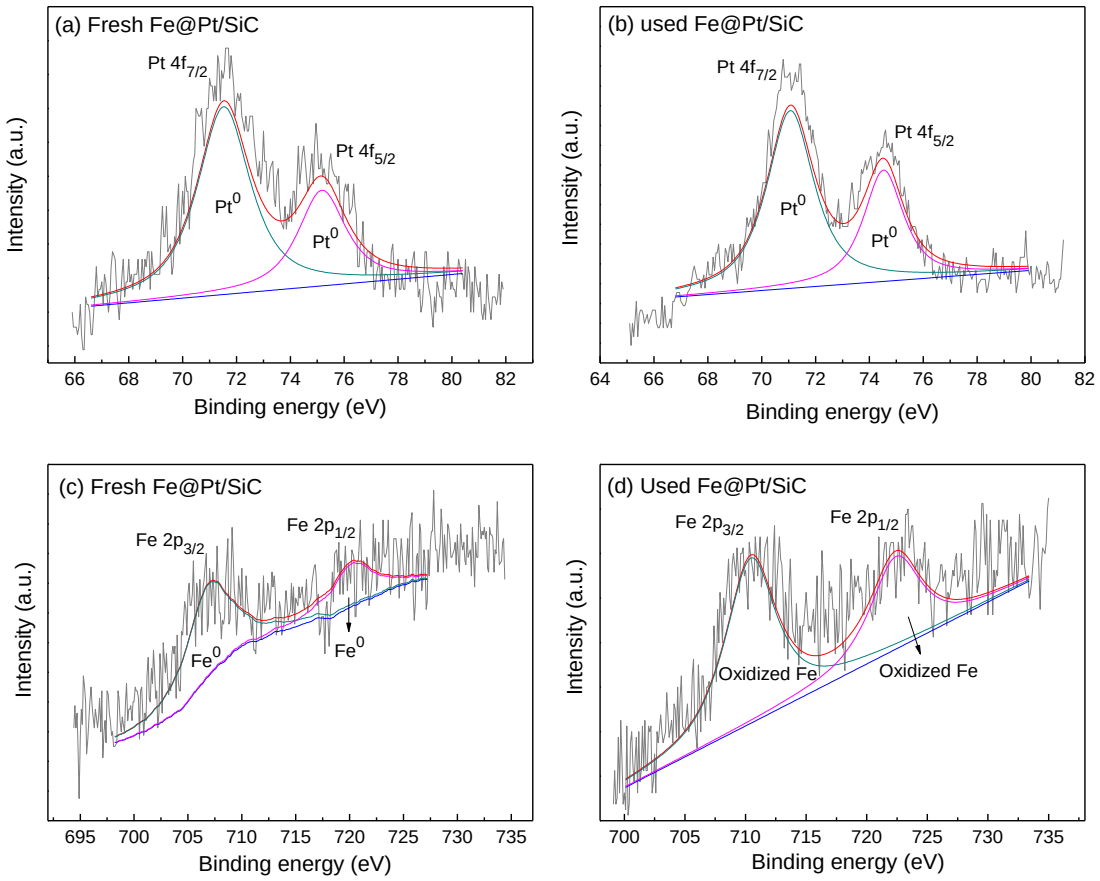

Fig.6 XPS spectra of Pt 4f (a and b) and Fe 2p (c and d) levels of fresh and used Fe@Pt/SiC.

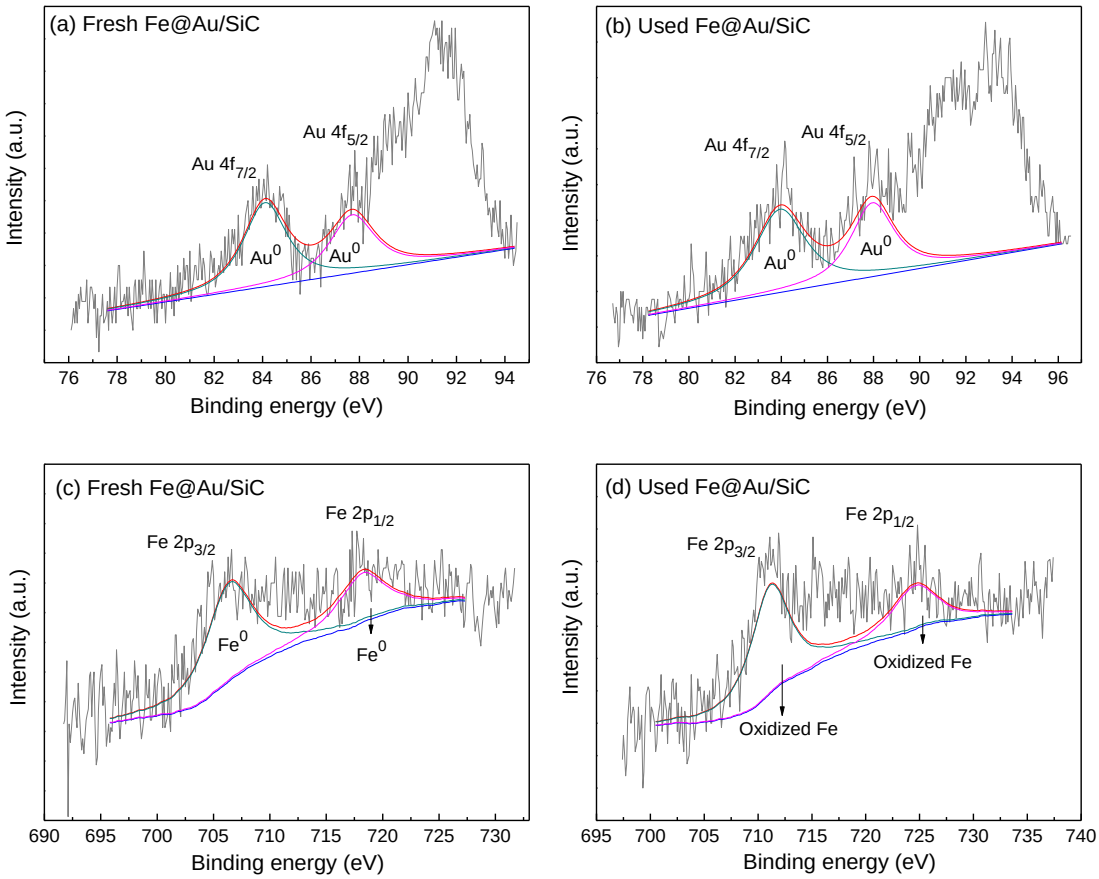

Fig.7 XPS spectra of Au 4f (a and b) and Fe 2p (c and d) levels of fresh and used Fe@Au/SiC.

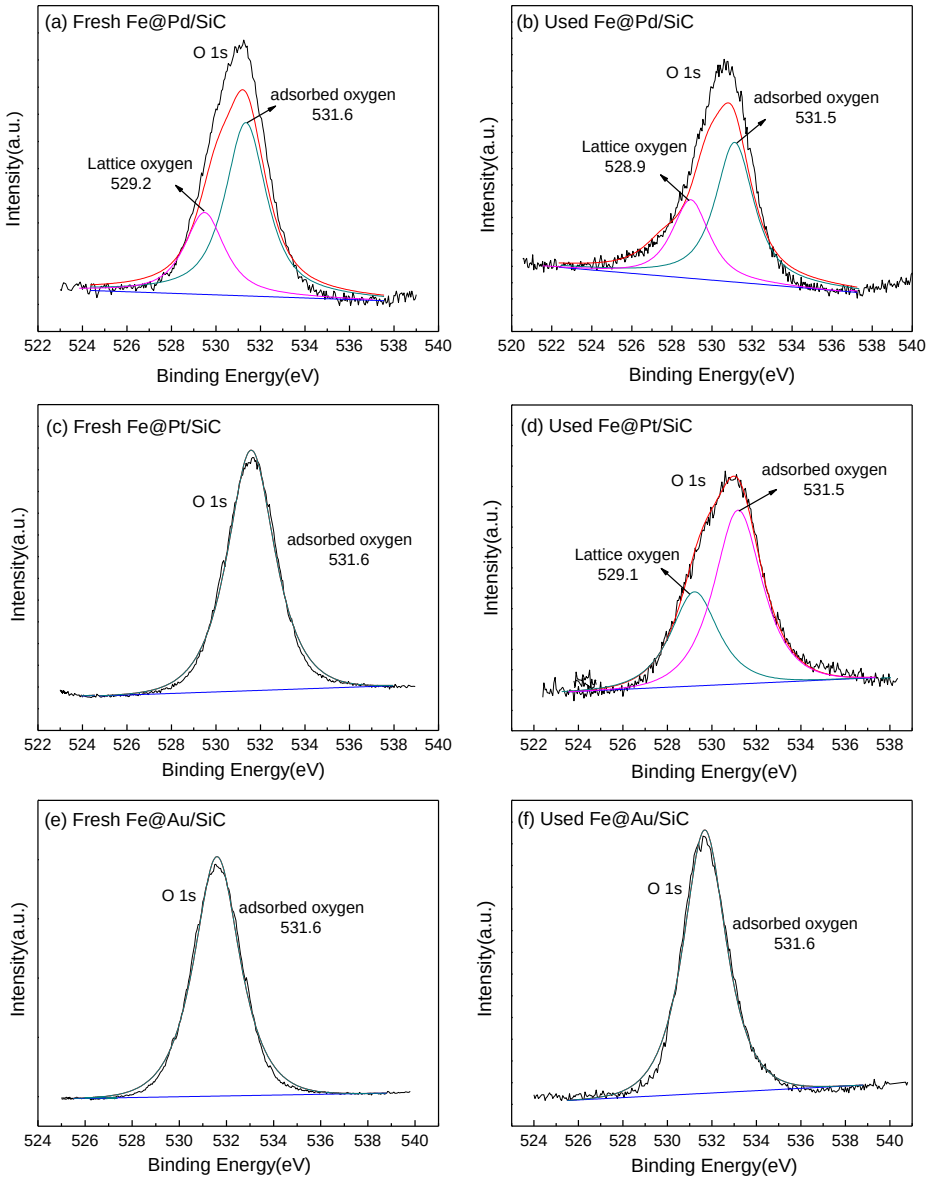

Fig.8 XPS spectra of O 1s levels of fresh and used Fe@Pd/SiC (a and b), Fe@Pt/SiC (c and d) and Fe@Au/SiC (e and f).